Investigations on the Near-Wake Region of a Generic Space Launcher Geometry

D. Saile*, A. Gülhan† and A. Henckels‡
DLR - German Aerospace Center, Cologne, North Rhine-Westphalia, 51147, Germany

The near-wake of a separated flow behind a generic space launcher model with different afterbody extensions is studied experimentally in the hypersonic flow regime (Mach number 6.0 and unit Reynolds number $16 \times 10^6\,\mathrm{m}^{-1}$) with the main objective being to show unsteady flow phenomena. This objective is based on the desire to control the base flow of space launchers to reduce drag and dangerous vibrations. The investigations focus on the unsteadiness of the base-pressure fluctuations and the oscillations of the recompression shock. Base-pressure spectra and spectra of the vertical recompression shock oscillation are discussed for various pressure transducer locations, various nozzle lengths and nozzle diameters. The base-pressure spectra exhibits dominant Strouhal numbers centered at 0.08 at the center positions and 0.08, 0.2, 0.38 at the outskirts of the base, and shows a crucial change with a frequency shift to Strouhal number of 0.27 when a nozzle is applied. Additionally, the pressure spectra indicate an azimuthal mode. The spectra of the recompression shock feature a dominant Strouhal number of 0.2 independent of the geometry of the afterbody. Since the incoming boundary layer is suspected to have an influence on the near-wake flow, the state and the flow conditions are examined in introductory experiments by means of infrared images of the model surface and Pitot pressure at the body corner.

Nomenclature

d	nozzle diameter
f	frequency
p	pressure
r	radial coordinate from center
x	axial coordinate from base
D	diameter of main body
L	nozzle length
U	axial component of the flow velocity
Ma	Mach number
Re	Reynolds number
Sr	Strouhal number
Φ	angle on base

Subscript

D	diameter of main body
pitot	Pitot pressure
rms	root mean square
∞	free stream condition

*Scientific employee, DLR - German Aerospace Center, Institute of Aerodynamics and Flow Technology, Supersonic and Hypersonic Technology Department (AS-HY, Linder Höhe, 51147 Cologne/Germany.
†Head of AS-HY, DLR - German Aerospace Center, Institute of Aerodynamics and Flow Technology, Supersonic and Hypersonic Technology Department (AS-HY), Linder Höhe, 51147 Cologne/Germany.
‡Scientific employee, DLR - German Aerospace Center, Institute of Aerodynamics and Flow Technology, Supersonic and Hypersonic Technology Department (AS-HY, Linder Höhe, 51147 Cologne/Germany.

I. Introduction

The subject of the study is the flow at the rear-end of axisymmetric bodies such as space launchers in the hypersonic regime. As a common denominator, the axisymmetric bodies feature an abrupt change in the geometry resulting in a wake with complex interactions of large coherent structures that determine the local and global behavior of the flow at the rear-end. To find indications of governing instability mechanism and relate them to the large coherent structures is the overarching goal. From the technical point of view, the understanding of governing mechanisms of instabilities are important for several reasons. The wake creates a specific drag due to a low-pressure level, which accounts for up to 35% of the total drag.[1] The unsteadiness of the wake induces an aerodynamic excitation with high aerodynamic loads, called buffet. Buffet can cause structural modes leading to buffeting and in the worst case scenario to the destruction of the excited component. Of special interest is the downstream reattachment of shear layer in the case of the presence of a solid wall like a nozzle. This causes high pressure loads and increased heat flux rates at the reattachment point and has to be taken into account in the design process of nozzles. An issue that is not discussed here, but affects the technical aspects of space launchers, concerns the interaction of the nozzle flow with the external flow. In this case, a vortex is induced along the shear layer of the nozzle flow that convects hot jets to the solid surface resulting in hot spots with high heat flux rates.[2,3]

The afterbody flow can be divided into distinct regions. At the rear-end, the incoming supersonic boundary layer and the outer inviscid flow feature a rapid expansion with the corresponding turning angle towards the axis due to the abrupt geometry change. A high energetic shear layer evolves from the corner, which subjects an adverse pressure gradient at a location further downstream generated from the realignment of the flow to the axis. Converging pressure waves emanate from this recompression region, which focus to a recompression shock. For the mean flow, a distinct reattachment location can be determined. The trailing wake is located downstream from the reattachment location. Upstream from there and enclosed by the base of the model and the free shear layer, is the location of the subsonic recirculation region.

Axissymmetric base flows have been subject of wide experimental and numerical investigations for over 50 years. Ref. 4, Ref. 5, Ref. 6 presented first experimental results for compressible subsonic flows on bodies of revolution. Ref. 7 examined supersonic base flows and emphasized the difference of the flow reattachment with and without the presence of a solid wall. More recently, the group around Dutton examined the supersonic flow at a blunt-based, axisymmetric model via Rayleigh/Mie scattering[8–10] and time-series base-pressure measurements.[11,12] The instantaneous planar Mie scattering images show large-scale structures in the shear layer. The time-series base-pressure measurements show dominant frequencies of the flutuactions equivalent to a Strouhal number of $Sr_D = 0.05$ for the center transducer and $Sr_D = 0.1$ for the outermost locations. Similar studies to the experiments shown here were executed by Ref. 13 on a generic model with representative nozzle extension for high subsonic flows. They found a distinct peak at a Strouhal number of $St_D = 0.08$ for the blunt body, $Sr_D = 0.18$ for a short nozzle within the recirculation region and a broad-band signal centered at $Sr_D = 0.1$ for a nozzle where the flow reattached. In subsonic afterbody investigations in the high subsonic regime on a detailed model of the Ariane V with two boosters on the side,[14] a distinct peak was found in the pressure spectra at $Sr_D = 0.22$ and a broad-band frequency centered at about Strouhal number of 0.5 to 0.6. Another dominant frequency at $Sr_D = 0.4$ is mentioned in comparable experiments in Ref. 15. In numerical investigations on the blunt-based axisymmetric model for a supersonic flow, Ref. 16 and Ref. 17 achieved to relate unstable modes to large coherent structures and Ref. 18 presented complementary numerical studies focusing on the shear layer flow. Numerical studies in the high subsonic region on base flows elongated with another cylinder were done by Ref. 19 and Ref. 20. The authors reported characteristic dimensionless frequencies at specific spatial location within the recirculation bubble. Almost all studies concerning the unsteadiness of the flow field observe Strouhal numbers at $St_D = 0.2$, which is often attributed to the absolute helicoidal unstable mode of the antisymmetric "shedding" instability within the recirculation region. Ref. 20 reports a coexistence of the shedding instability with a "flapping" instability. It was found that flapping of the shear layer is convectively unstable and associated with $Sr_D = 0.08$. In two-dimensional flows, it is reported to describe the overall growth and decay mechanism of the recirculation region. Another predominant Strouhal number in the literature is $Sr_D = 0.6$. Vortical structures in the free shear layers that break into smaller scales in the recompression region are mostly referred to that number.

The organization of this contribution is as follows: The experimental set-up is briefly described in Chap. II. Then, the experimental results are shown in Chap. III, which is divided into a first part that shows experiments to the incoming boundary layer (Chap. A) and a second part that addresses the unsteady base-pressure measurements (Chap. B). The conclusions are given in Chap. IV.

II. Experimental Facilities, Windtunnel Model and Measurement Technology

Measurements were performed in the supersonic wind tunnel H2K at the Institute of Aerodynamics and Flow Technology in the Supersonic and Hypersonic Technology Department located in Cologne. The wind tunnel H2K is a blow-down type wind tunnel equipped with a vacuum sphere to reach high Mach numbers. Six different aerodynamic testing nozzles are available reaching from Mach number 4.8 to 11.2. An electric heater can heat the air in the stagnation chamber up to 1100 K to adjust the Reynolds number. For the experiments presented here, the facility was operated at a stagnation pressure of 18 bar and a stagnation temperature of 470 K at a freestream Mach number of 6.0, which generates a unit Reynolds number of $16 \times 10^6\,\mathrm{m}^{-1}$.

Experiments were carried out on a generic model (Fig. 1), which represents the Ariane 5 configuration with respect to the main geometrical bodies. The exterior geometry is an assembly of simple geometrical bodies called reference configuration B.A (other configurations are investigated in other groups of the project within the framework of the DFG SFB-TR40). It consists of a spherical nose with a radius of 10 mm that is attached to the cylindrical main body with a diameter of 108 mm and a length of 328.6 mm via the cone with an opening angle of 36°. The strut attached to the wind tunnel model is defined by a front wedge with an opening angle of 30°, a shaft with a width of 22 mm and a length of 156 mm and rear wedge with an opening angle of 20°. The reference configuration B.A was modified during the experiments by mounting cylinders at the base to simulate a geometric representative of a nozzle. No nozzle flow was applied. Nozzle lengths of $L/D = 0, 0.5, 1.0, 1.2$ were investigated while keeping the diameter at $d/D = 0.4$ and, in a next step, the diameter was increased from $d/D = 0.4$ to 0.7 by increments of 0.1 while keeping a length of $L/D = 1.2$. In order to trigger the transition of the boundary layer to a turbulent state, four tripping configurations have been applied successively using carborundum with a grain size of 400 μm and a zigzag-tape of the same height as tripping elements. First, a ring of carborundum with a width of 5 mm was applied on the nose at 45.4 mm (conf. 1) measured from the tip of the nose along the symmetry axis. Then, a second ring was added at 201.4 mm (conf. 2) on the cylindrical main body. Later, another ring was added at 352.4 mm (conf. 3). At last, the two rings on the main body were removed and replaced by a zigzag-tape at 201.4 mm (conf. 4). In experiments described in Chap. A, all tripping configurations have been used. After having made the experience that the tripping elements had little influence on the base-pressure behavior (Chap. 1), the following experiments have been executed with tripping conf. 3 and conf. 4.

Steady and unsteady measurement techniques were applied. For the measurements concerning the boundary layer, the Pitot pressure was measured with a Pitot rake mounted at the end of the blunt base (see Fig. 2). In order to incorporate the full boundary layer thickness, the rake was elevated in a second run. Each pressure tube was connected to a 15psi pressure scanner of Esterline Pressure Systems containing piezoresistive sensors and read with a system 8400 pressure data acquisition unit. The measurement uncertainties are 0.1% for full scale. Additionally, infrared images were taken with a ThermaCAM SC3000 NTS camera of Agema. In order to measure the unsteady behavior of the recompression shock behind the base, a high-speed schlieren technique was applied using an Ultima APX-RS camera of Photron. It contains a 10 bit CMOS sensor, which provides a resolution of 1024×1024 pixel at a frame rate of 3000 fps and a maximum frame rate of 250000 fps at reduced resolution. The recompression shock was recorded with 16800 fps and 20000 fps, that resulted in 35000 to 50000 frames depending on the resolution. High-frequency pressure measurements were obtained with Kulite differential XCQ-080 pressure transducers, which feature typically a combined non-linearity, hysteresis and repeatability of 0.1%. Six pressure transducers with a pressure range of 0.35 bar were flush mounted in plugs of the base (see Fig. 3) where they were held in place with O-rings. The pressure reference tubes were connected to the ambient pressure of the measurement chamber. A GBM Viper system is used for the data acquisition purposes. The data was acquired over 10 s with a sampling rate of 96000 Hz. The cut-off frequency was set internally by the data acquisition system to 48000 Hz.

Infrared images show only qualitative results, which refers to the fact that the material of the wind tunnel model is black-painted steel, meaning that the material features a high temperature conductivity and an unknown emission coefficient. For this reason no heat flux can be derived and fine structures derived from transitional phenomena in the boundary layer cannot be resolved. But the qualitative temperature distribution reveals the transition location, and additionally gives insights to the disturbance effects coming from the strut holding the model. For the measurements with the Kulite pressure transducers, a radial and a reference arrangement was used. Fig. 4 shows the radial arrangement with the transducers on the opposite side of the strut ($\Phi = 0°$) on a radius r at $0, 12, 25, 35, 45, 50$ mm. Measurements described in Chap. 1 were conducted with this arrangement. For the measurements discussed in Chap. 2, the transducers were still

radially aligned, but with an angle of $\Phi = 225°, 270°, 315°$. Fig. 5 displays the reference arrangement (used for measurements in Chap. 3 and Chap. 4), that was defined in accordance with the partners of the SFB-TR40. The transducers were distributed angularly at a radial distance of $r = 40\,\text{mm}$ at $\Phi = 170°, 180°, 190°, 210°$ and 240°. Additionally, another transducer was placed at $r = 30\,\text{mm}$ and $\Phi = 180°$.

Figure 1. Wind tunnel model

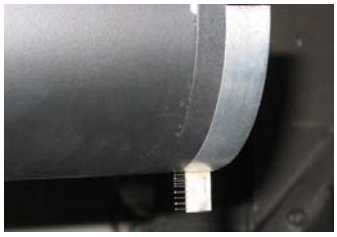

Figure 2. Pitot rake mounted on afterbody

Figure 3. Instrumentation of base

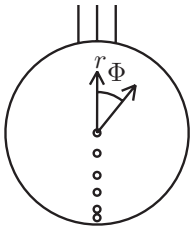

Figure 4. Radial pressure transducer arrangement

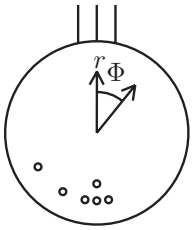

Figure 5. Reference pressure transducer arrangement

The unsteady measurements from the high-speed camera and the pressure transducers were both analyzed using the fast Fourier transform algorithm (FFT). In the case of the high-speed schlieren measurements, the vertical position of the shock was gained by analyzing the intensity profile at a defined location for each image.[21] Then, the data sequence was segmented into sets of 1024 with an overlap of 50%, multiplied with a Flattop window to suppress side-lobe leakage. For the pressure transducers, segments of 8192 samples with an overlap of 50% were used in combination with a Hanning window.
The high-speed schlieren image sequence of the recompression shock was additionally processed by determining the standard deviation of the gray values of each pixel within the sequence. The result is an image that shows the zonal deviation of the shock from the mean. Pixels with a lighter gray have a higher deviation from the mean than pixels with a darker gray. The mean location of the recompression shock was derived with that method.

III. Experimental Results

The experimental results are devided into two parts. Chap. A examines the state of the boundary layer on the cylindrical part of the model using an infrared camera and a Pitot rake. Experiments with different tripping configurations were conducted in order to study the laminar-turbulent transition of the boundary layer. Chap. B focuses on the unsteady phenomena behind and at the base. The results of the high-speed schlieren and the unsteady pressure measurements are presented for different afterbody configurations.

A. Introductory Measurements to the State and Conditions of the Boundary Layer

Introductory wind tunnel tests were run at the end of the cylindrical part of the model to determine the state and the Pitot profile of the boundary layer. The color code goes from blue to red whereas red indicates a higher temperature. On one hand, this is important in order to have a well-defined problem including the influential parameters for the base flow, and on the other hand, to provide input parameters for numerical

studies. The question concerning the state of the boundary layer was addressed with an infrared camera taking an image of the qualitative surface temperature along the cylindrical surface of the model (see Fig. 6). Fig. 6 shows the infrared image for the tripping with three rings of carborundum (see Chap. II). Following the flow from the first tripping element on the main body, two patterns in a V-shape can be observed on the surface indicating two growing longitudinal vortices. One can also see that the strut triggers a temperature rise that travels from the arm around the whole cylinder. The evident line of color change is considered to be the laminar-turbulent transition location. The footprint of the two observed vortices disappear behind this line and behind the last tripping element the temperature distribution appears to be homogenous leading to the assumption that the flow is fully turbulent at the base.

This assumption is backed up by the measurements of the Pitot rake. Fig. 7 depicts the Pitot pressure profile of the boundary layer taken on the opposite side of the strut at the end of the cylindrical main body. In comparison to the experiments, a two-dimensional numerical simulation RANS on an axisymmetric geometry was executed with corresponding initial conditions applying the $k-\omega$ turbulence model. The Pitot pressure from the numerical simulation is plotted in the same figure. The experimental data agrees well with the numerical results with respect to the curvature and the final thickness of the boundary layer. The transition to the ambient Pitot pressure is less sharp for the numerical simulation. This finding was observed before and is due to the chosen turbulence model. The experimental results also depict a decreasing Pitot pressure for an increasing radial distance. Investigations have shown that this is caused by a shock induced slip line from the first tripping element on the bow shock of the nose. For a better understanding, the velocity profile of the numerical simulation is also plotted in the graph. Additional Pitot pressure measurements were taken for different angular locations which are not presented here. The common observations of these additional measurements is that the boundary layer along the cylinder resembles in a range of 45° on the opposite side of the strut the boundary layer of an undisturbed flow. At locations closer to the strut the boundary layer exhibits major deviations to the commonly known profiles of turbulent boundary layers.

The infrared and the Pitot pressure measurements display both the typical characteristics of a hypersonic turbulent boundary layer. However, in sub-project B4 infrared measurements have been conducted in the Hypersonic Ludwieg Tube (HLB) at TU Braunschweig with comparable flow parameters on a wind tunnel model made of PEEK. As a consequence of the conductivity of the material, a better resolution can be achieved. These results show a similar behavior concerning the location where the increase of the temperature sets in and, thus indicates a comparable transition location. However, streaks of higher temperatures reaching up to the end of the cylindrical main body were observed, meaning that the vortices did not grow and merge. Further investigations will be conducted in this sub-project in order to clarify if the boundary layer can actually be considered to have the characteristics of a hypersonic turbulent boundary layer.

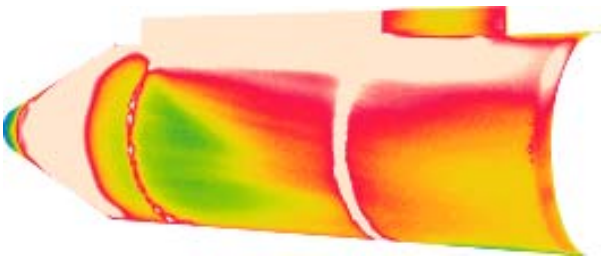

Figure 6. Infrared image for tripping configuration (conf. 3)

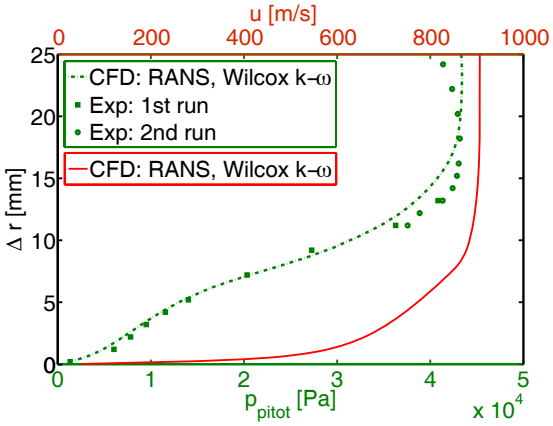

Figure 7. Pitot pressure profile (green) from a CFD simulation and experiments at the opposite side of the strut and velocity profile from the same CFD simulation (red)

B. Fluctuation Measurements in the Base Region

Two flow regions behind the base are investigated: the recirculation zone is examined concerning the pressure fluctuations and the recompression zone is observed by analyzing high-speed schlieren images. Both measurement methods are applied to different configurations of the model: to the reference configuration B.A and to configuration B.A that is modified by adding nozzles of different diameters and lengths. Chap. 1 describes the influence of the different tripping configuration on the pressure fluctuations for reference configuration B.A. In the Chap. 2, the investigations on configuration B.A is extended to examine the spatial surface resolution of the pressure fluctuations on the base. Chap. 3 and Chap. 4 contain observations about the pressure fluctuations for different nozzle lengths and the nozzle diameters, respectively. The results concerning the fluctuations of the high-speed schlieren technique are mostly discussed in Chap. 3 and Chap. 4.

1. Reference Configuration B.A - Variation of the Tripping Configurations

In the following, the base-pressure spectra is discussed for the radial arrangement of the transducers (Fig. 4) with respect to its main characteristics and the sensitivity to the different tripping configurations. Fig. 8 shows the pressure spectra for the four different tripping configuration. The pressure fluctuations p_{rms} are plotted in the z-direction as rms value in Pascal over the Strouhal number Sr_D. The Strouhal number is defined according to $Sr_D = fD/U_\infty$ by using the diameter of the main body as characteristic length scale. First, one can see that all curves are coherent featuring the same characteristics. Describing the pressure spectra for each transducer from the center with increasing radial distance, the following observations can be stated: the center transducer at $r = 0\,\text{mm}$ exhibits the highest level of pressure fluctuations with a peak at $Sr_D = 0.05$, a side peak at $Sr_D = 0.08$ and some broad frequency content at $Sr_D = 0.2$. The fluctuation energy is distributed up to $Sr_D = 0.8$. For the next transducer at $r = 12\,\text{mm}$, the overall pressure fluctuation level decreases while the pressure peak at 0.08 is still notable. As before some energy content is contained at $Sr = 0.2$. At $r = 25\,\text{mm}$, the peak at 0.08 continues to decrease and pressure fluctuations centered at 0.2 are more present. The last three transducers located closer to the separation corner at $r = 35, 45, 50\,\text{mm}$ show a highly coherent behavior. The level of the pressure fluctuations centered at 0.08 decreases further and the elevation at 0.2 is now more prominent. Furthermore, a distinct elevation centered at 0.38 can also be discovered.

A last note is dedicated to the peaks that the transducer at $r = 35, 45$ exhibit. These peaks are suspected to be caused by electrical interferences and not by the flow. On one hand the same transducers show the same peaks at different locations, and on the other hand, the neighboring transducers do not show a similar peak in the spectrum.

By summing up these observations one can derive four major conclusions. All curves coincide, thus the tripping elements have little or no influence on the pressure spectra. Concerning the spatial pressure level distribution, most of the pressure fluctuation energy is contained in the middle of the base centered at a Strouhal number of $Sr_D = 0.08$. The outskirts features three dominant non-dimenionsal frequencies centered at $Sr_D = 0.08, 0.2, 0.38$. The coherent behavior of the outer transducers give rise to the assumption that the unsteady flow topology is divided in an inner region and an outer region. It seems as though the inner region is governed by effects at $Sr_D = 0.08$, which is often related to the overall growth and decay mechanism of the flow (flapping), while the outer region seems to be influenced by flapping, shedding ($Sr_D = 0.2$) and another effect, which shows a periodicity of $Sr_D = 0.38$.

In literature, no reference was found to coherent structures with a characteristic Strouhal number $Sr_D = 0.4$. Ref. 11 and Ref. 12 reported in their base pressure measurements similar results. A concentration of the pressure fluctuations in the center with a frequency shift closer to the outskirt. The dominant Strouhal numbers were equivalent to $Sr_D = 0.05$ in the center and $Sr_D = 0.094$ further outside. In supersonic numerical investigations of Ref. 18 at $Ma = 2.46$, a pressure spectra close to the base and in the shear layer ($x/R = 0.25$,$y/R = 0.97$) was shown. The authors discuss peaks at $Sr_D = 0.96, 0.144$ and the graph reveals, amongst other frequencies, also a peak at about 0.2.

2. Reference Configuration B.A - Variation of the Pressure Transducer Position

The question concerning the spatial pressure spectra distribution is addressed by varying the angular position of the transducers (Fig. 9). An observation that is common for all angles Φ of the radial transducer alignment concerns pressure level. The overall level of the fluctuations are about the same for the same radial distances: the fluctuations in the center region are the highest in the center region with a periodicity of 0.05 and 0.08 and

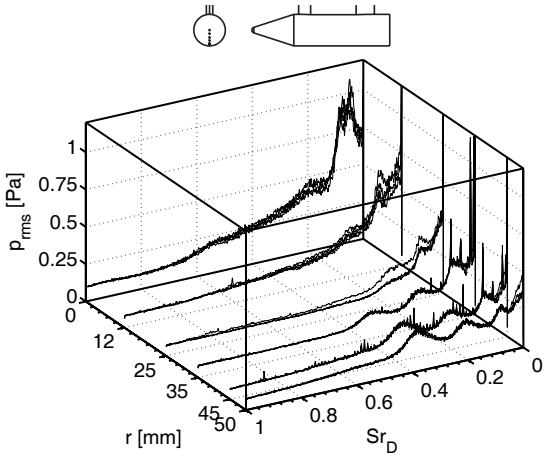

Figure 8. Pressure spectra for different tripping configurations (conf. 1 to conf. 4). Pressure transducers a radially aligned at an angle of $\Phi = 180°$.

decrease towards the outer region. Additionally, the outer three transducers exhibit a dependency to their angular orientation. As discussed before, the spectra for outer transducers with the alignment of $\phi = 180°$ shows fluctuations centered at $0.08, 0.2$ and 0.38. Changing the angular alignment now results first in a flat spectrum for the outer transducers ($\Phi = 225°$ and $270°$), then, for $\Phi = 315°$, the well-known dominant Strouhal numbers at $Sr_D = 0.08$ and 0.2 can be discovered again.

There are two possible explanations for the azimuthal dependency of the pressure fluctuations. Either it is simply the influence of the strut that alters the base flow to a preferred orientation preventing a free organization of the flow, or that there exists an azimuthal mode on the base with areas of high pressure fluctuations with a dominant Strouhal numbers. The explanation that it is caused by the strut is supported by the observations of Ref. 11 where the authors see no azimuthal dependency for the transducers distributed angularly close to the edge at $r/R = 0.84$. On the other hand, numerical investigations with a jet in the hypersonic regime[2] revealed this azimuthal organization of the flow. Finally, the hypothesis of azimuthal pressure fluctuation waves can only be resolved with a higher spatial resolution of the pressure fluctuations on the base.

3. Geometric Variation - Variation of the Nozzle Length

The experiments described here investigate the geometric dependencies of the base-pressure fluctuations to the presence of an extension that simulates the outer geometry of a nozzle. A nozzle flow was not applied. The transducers are now situated according to the reference arrangement (Fig. 5). First, comparisons related to the pressure spectra of the radial and the reference arrangement of the transducers are drawn. Then, the emphasis lays on showing the differences in the pressure spectra when nozzles of different lengths are added to the base. Furthermore complementary results received from the high-speed schlieren measurements are presented.

Fig. 10(a) shows the second set of base-pressure spectra to the reference configuration B.A. The first set of base-pressure spectra was shown in Chap. 1 and Chap. 2 with a radial transducer arrangement. The wavy course of the spectra with dominant Strouhal numbers with the centers at $0.08, 0.2, 0.38$ can be discovered again at $\Phi = 170°, 180°, 190°$. At an angle of $\Phi = 210°$, the signal is broader, meaning the dominant frequencies are less pronounced. This trend continues for $\Phi = 240°$ where non of the non-dimensional frequencies can be found anymore. Instead, pressure fluctuations with a periodicity of 0.035 appears at $\Phi = 210°$ and $240°$. Next, a nozzle of $L/D = 0.5$ is attached to the base. The pressure spectra in Fig. 10(b) depicts that the dominant Strouhal number is now shifted to $Sr_D = 0.16$ clearly visible at $\Phi = 170°, 180°, 190°$, and that the overall level of the pressure fluctuations increases. Other frequencies than this disappear. Elongating the nozzle length to $L/D = 1.0$ leads to another frequency shift to $Sr_D = 0.27$ (see Fig. 10(c)) and again to an increase of the pressure fluctuations. Furthermore, it can be seen that more energy is contained in the

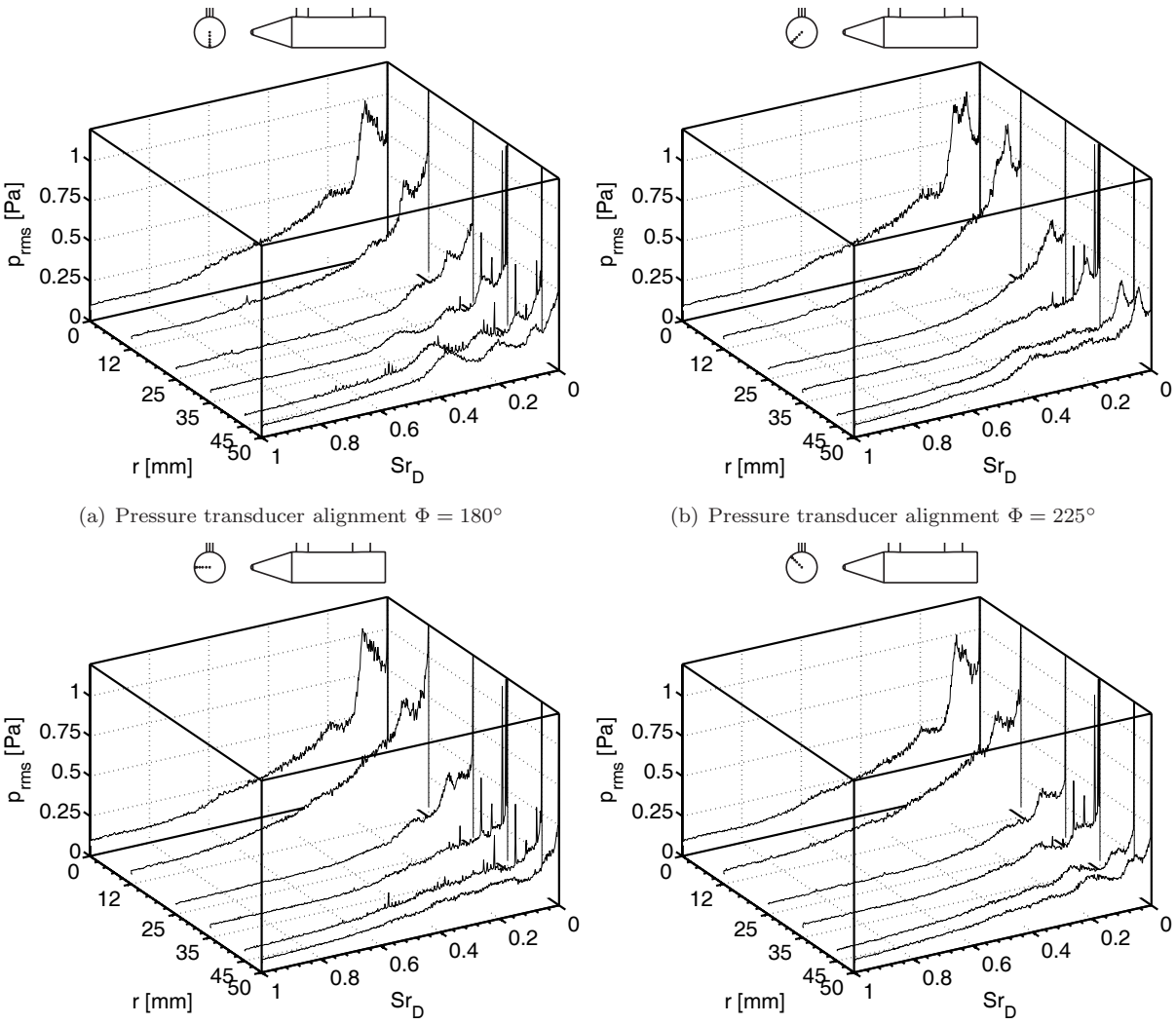

(a) Pressure transducer alignment $\Phi = 180°$

(b) Pressure transducer alignment $\Phi = 225°$

(c) Pressure transducer alignment $\Phi = 270°$

(d) Pressure transducer alignment $\Phi = 315°$

Figure 9. Pressure spectra for radial pressure transducer alignment at different angles Φ

lower frequency region between $Sr_D = 0$ and 0.1. No change concerning the course of the pressure spectra is caused by the elongation of the nozzle from $L/D = 1.0$ to 1.2, which can be seen in Fig. 10(d). A common feature of all spectra shown in Fig. 10 is the dependency of the base-pressure fluctuations to the azimuthal location. The high pressure fluctuation level at $\Phi = 180°$ with its characteristic Strouhal number decreases with an increasing angle whereas the signal becomes flatter.
Without a nozzle extension, the base flow features mainly three different non-dimensional frequencies that can possibly be related to flapping ($Sr_D = 0.08$), shedding ($Sr_D = 0.2$) and another instability mode ($Sr_D = 0.38$). After applying a nozzle extension, only one dominant frequency can be detected. The reason might lay in the suppression of the antisymmtric movements of the wake.

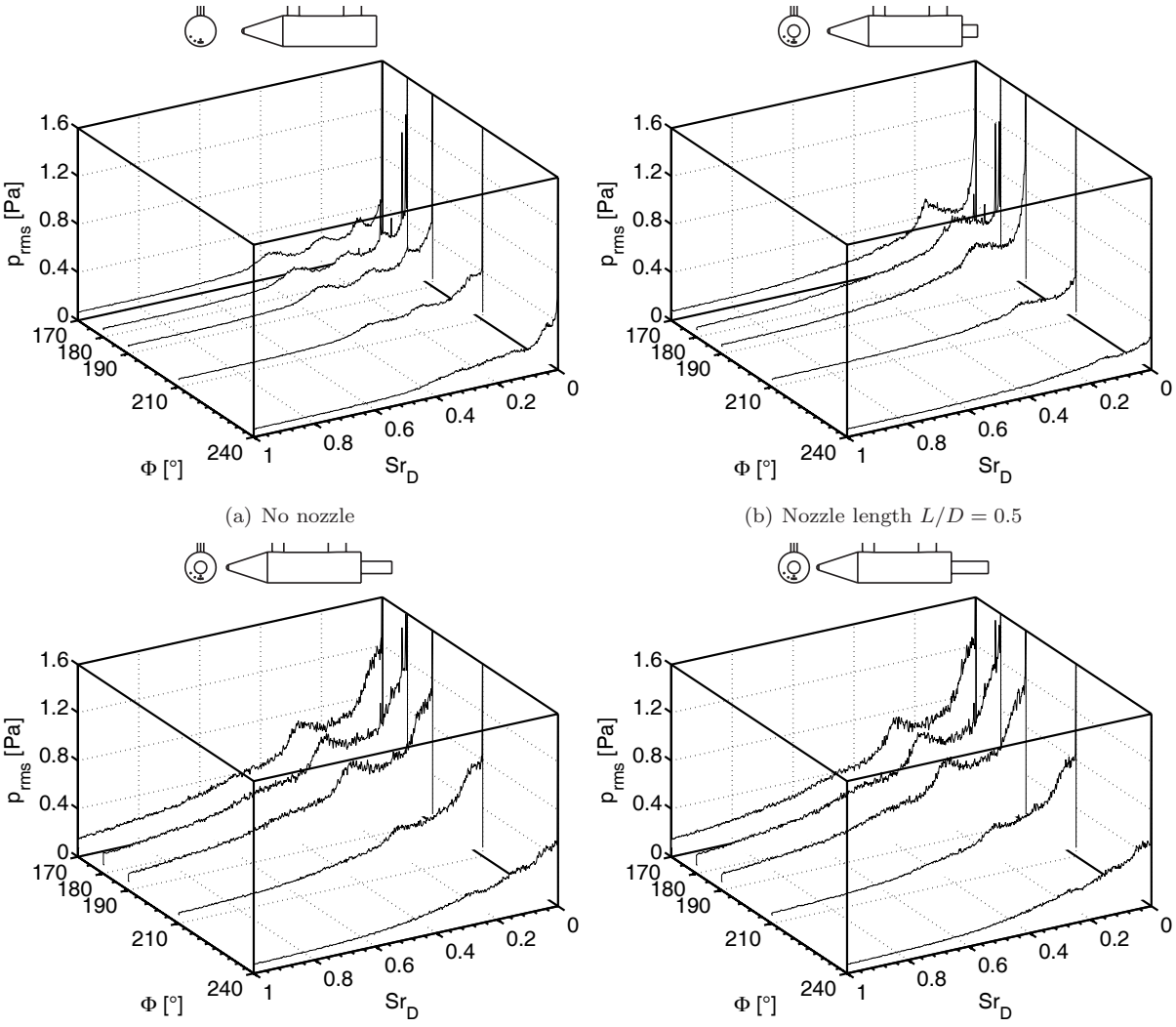

(a) No nozzle

(b) Nozzle length $L/D = 0.5$

(c) Nozzle length $L/D = 1.0$

(d) Nozzle length $L/D = 1.2$

Figure 10. Pressure spectra for different nozzle lengths L. The nozzle diameter is $d/D = 0.4$.

Further insights into the behavior of the base flow can be derived by analyzing the high-speed schlieren images. As discussed in Chap. II, the mean of the recompression shock location is calculated by using the standard deviation of the high-speed schlieren image that results in an image exemplarily shown in Fig. 11. The same method was applied to determine images for other afterbody geometries. The location of the mean recompression shock is given in Fig. 12 for different nozzle lengths. The origin of the coordinate system is located in the center of the base. The axis of abscissa x/D represents the distance along axial-symmetric axis and the ordinate describing the radial distance r is set perpendicular. The recompression shock for the

nozzle length $L/D = 1.0$ and $L/D = 1.2$ coincide exactly. One can see that the recompression shock for the nozzle with a length of $L/D = 0.5$ features a kink at $x/D \approx 1.3$ before it coincides with the course of the recompression shock location for the model configuration with no nozzle. Additionally, the standard deviation image can be used to estimate aspects of the dynamics of the recompression shock. Fig. 11 shows exemplary for the nozzle with $L/D = 1.2$ and $d/D = 0.4$ that the standard deviation of the shock position is evenly distributed below and above the mean location of the shock with no knots. The vertical deviation is estimated to be about 2.5 mm. Complementarly, Fig. 13 plots the vertical amplitude spectra. All afterbody configurations shown here feature a dominant Strouhal number that centers at $Sr_D = 0.2$ (high-speed schlieren sequence for nozzle geometry $L/D = 1.2$ was only available with a resolution of $3000 fps$). More detailed investigations (not presented here) have shown that the dominant Strouhal number is also independent of the location, meaning the Strohal number $Sr_D = 0.2$ stays constant along the recompression shock.

Some conclusions that can be drawn from the observations in this chapter are congruent with the one discussed in Chap. 2. With the same reasoning, the azimuthal dependency of the pressure spectra can either be caused by the strut or the azimuthal wave. Due to the comparable course of the spectra 10° to the left and right of the transducer at 180°, the spectra suggest that the measured base flow is symmetrical to plane of the strut. This indicates that the strut generates a preferred orientation within the base flow. The striking similarities of pressure spectra for the nozzle $L/D = 1.0$ and $L/D = 1.2$ relies on the same location of the mean recompression shock. A further lengthening of the nozzle has no impact to the base-pressure fluctuations. Another way to look at it is based on the explanation of the physical effects. At the shoulder of the model, the flow is deflected towards the axis due to the expansion and experiences further downstream a recompression induced by the realignment of the flow along nozzle. As a result, the recirculation region contains an identical volume, hence identical conditions in the recirculation region. The recompression and the associated realignment of the flow for the configuration with no nozzle takes place due to the approach of the flow to the axis of symmetry, which differs crucially from the reattachment mechanism on a solid surface. This finding is also captured in the pressure spectra. An intermediate state for the reattachment mechanism was caught with the nozzle length $L/D = 0.5$. For the base flow with the nozzle length $L/D = 0.5$, the flow is forced to undergo two sequences of expansion and realignment leading to two regions where shock waves are emanated. The shocks interact at location $x/D \approx 1.3$ resulting in a course that coincides downstream from that location with the no nozzle configuration. Overall it can be stated that the introduction of a nozzle has a massive impact on the base flow resulting in a shift to one characteristic higher frequency and to a higher pressure fluctuation level. However, the oscillations of the recompression shock remain constant at $Sr_D = 0.2$ independent of the nozzle length.

In literature, the findings concerning the recompression shock oscillations are backed up by Ref. 3 who conducted similar experiments with an exhausting jet. The authors found oscillations of the inner shock with a non-dimensional frequency equal to 0.2. Ref. 19 studied high subsonic axisymmetric base flows with a nozzle. Here, the shedding of the entire recirculation bubble happens with a dimensionless frequency of about 0.2.

4. Geometric Variation - Variation of the Nozzle Diameter

The transducer arrangement was kept according to Chap. 3. Fig. 10(a), Fig. 10(d), Fig. 14(a), Fig. 14(b) and Fig. 14(c) depict the pressure spectra where the diameter was increased according to $d/D = 0, 0.4, 0.5, 0.6, 0.7$ while the length stayed constant at $L/D = 1.2$. Increasing the nozzle diameter from $d/D = 0.4$ to 0.5 causes a reduction of the elevation of the pressure fluctuation at the distinct non-dimensional frequency $Sr_D = 0.27$. The development to a broader signal with no distinct elevation continues when the nozzle diameter is increased again to $d/D = 0.6$ and is accompanied by an overall reduction of the signal. For $d/D = 0.7$, the level of the pressure fluctuations is reduced further. As already seen in Chap. 3, the pressure spectra of Fig. 14(a) and Fig. 14(b) features an azimuthal variance. Overall, one can see that by increasing the nozzle diameter, the level of the pressure fluctuations first grow, then reach a maximum and finally decrease. It suggests that the recirculation region gets excited with the introduction of a nozzle, but "dies" if more space of the recirculation region is used by the nozzle. The recirculation region contains a distinct Strouhal number at $Sr_D = 0.27$.

The recompression shock location moves closer to the rear end of the model when the diameter of the cylinder is increased because the axial realignment is forced to set in earlier. The location of the recompression shock is plotted in Fig. 15. Fig. 14 shows the spectrum of the vertical position fluctuations. As seen before, the

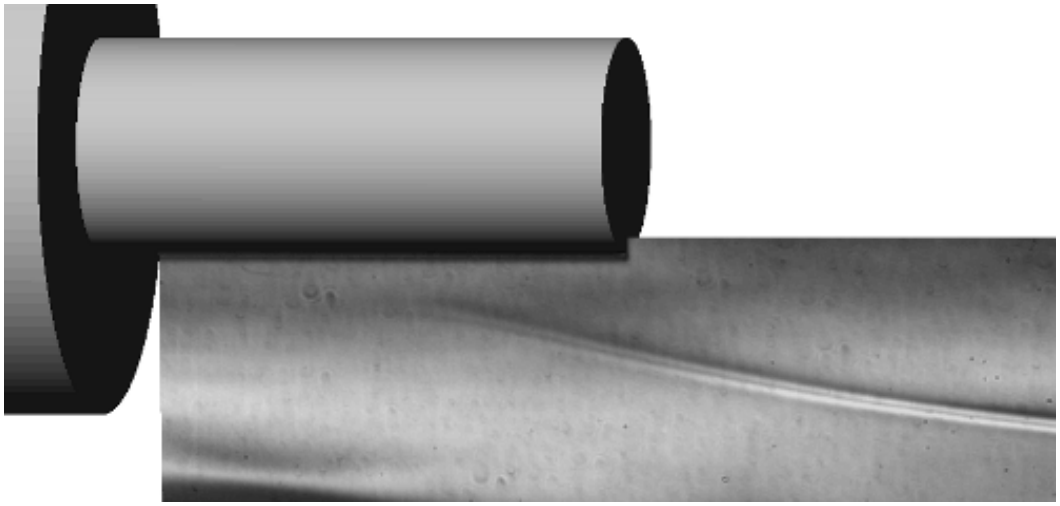

Figure 11. Standard deviation of a sequence of high-speed schlieren images of the recompression shock exemplary for a nozzle length of $L/D = 1.2$ and a diameter of $d/D = 0.4$

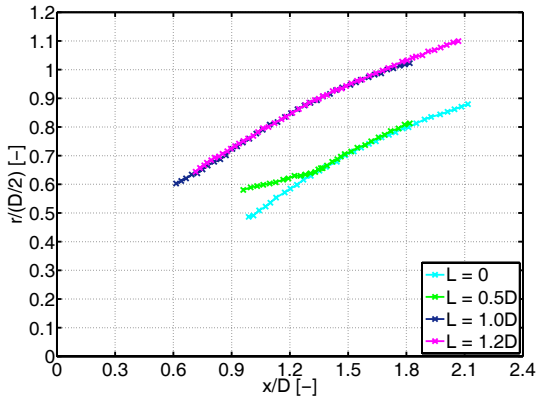

Figure 12. Mean recompression shock location for different nozzle lengths L. The nozzle diameter is $d/D = 0.4$.

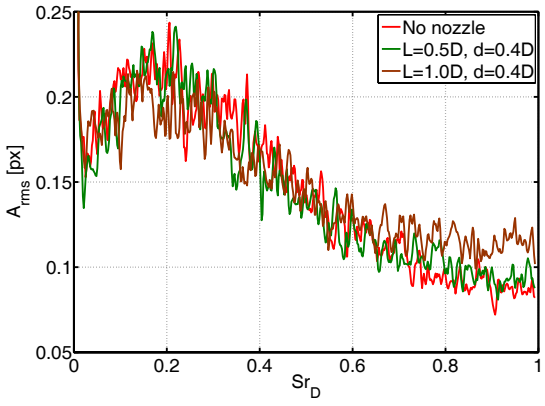

Figure 13. Spectrum of the oscillating recompression shock for different nozzle lengths

dominant Strouhal number centers around $Sr_D = 0.2$.

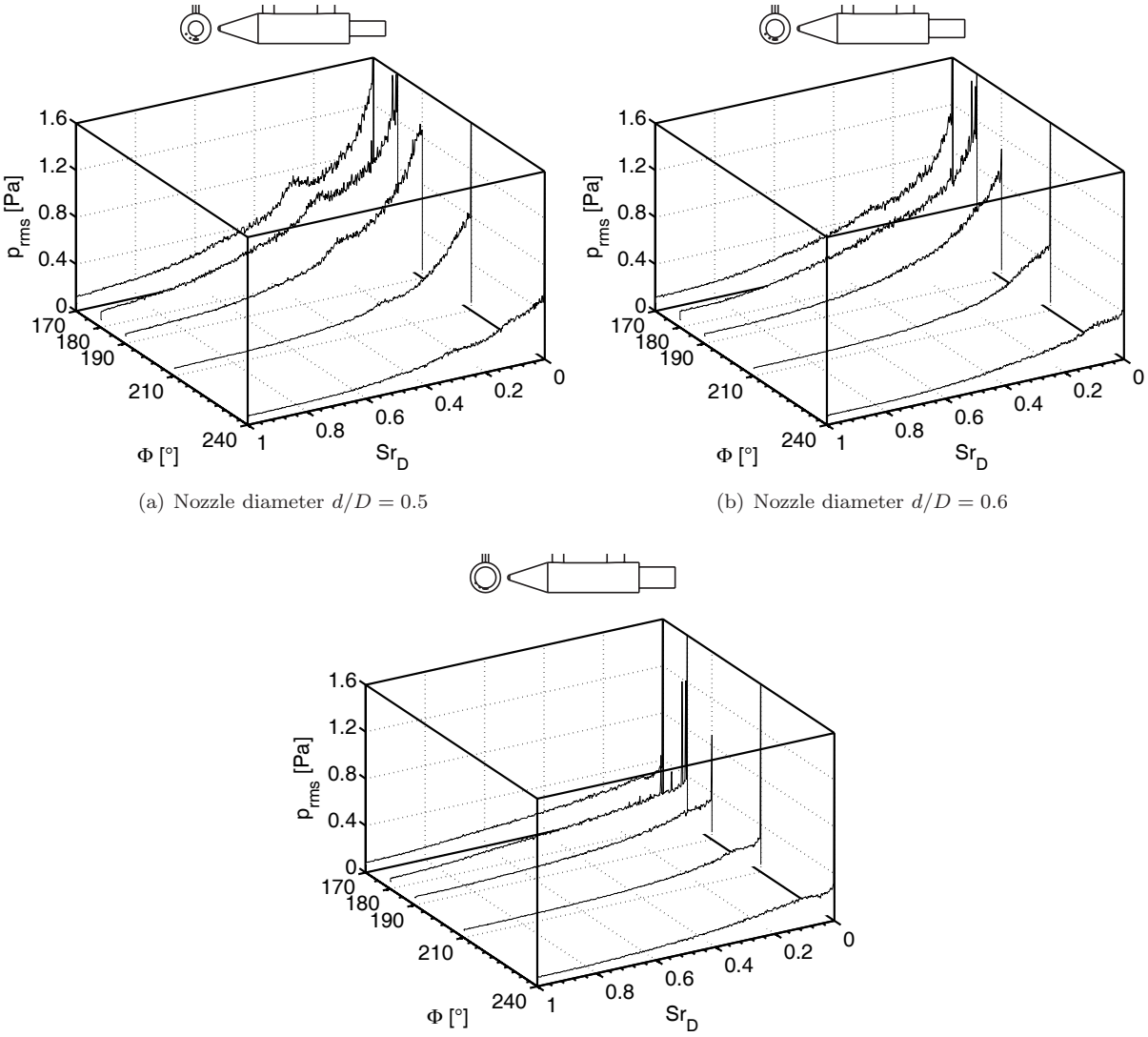

(a) Nozzle diameter $d/D = 0.5$

(b) Nozzle diameter $d/D = 0.6$

(c) Nozzle diameter $d/D = 0.7$

Figure 14. Pressure spectra for different nozzle diameters d. The nozzle length is $L/D = 1.2$.

IV. Conclusions

In the present work, axisymmetric base flows have been investigated at $Ma = 6$ and $Re_D = 1.7 \times 10^6$ for different afterbody extensions. Introductory experiments have been presented to determine the boundary conditions as much as possible. Next, results of unsteady base-pressure measurements have been discussed and complemented with unsteady high-speed schlieren measurements. A direct comparison of the data is difficult because little reference data are available for unsteady measurements conducted in the hypersonic regime on an axisymmetric base. But it is shown that the data is reproducible for different runs.
The unsteady base-pressure measurements revealed dominant Strouhal numbers centered at $0.08, 0.2$ and 0.38 for the configuration without a nozzle. The base pressure fluctuations features a shift to $Sr_D = 0.27$ and a higher pressure level when the reattachment takes place on a solid surface like a nozzle. This indicates a change of the flow topology. An increase of the nozzle diameter results first in an increase in the pressure fluctuation level with a distinct Strouhal number followed by a decrease. From the technical point of view, this behavior indicates that a diameter ratio with maximal loads exists. Thus, an unfavorable ratio, which is

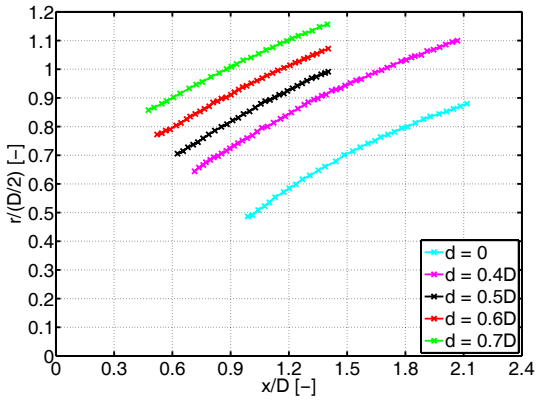

Figure 15. Mean recompression shock location for different nozzle diameters d. The nozzle length is $L/D = 1.2$.

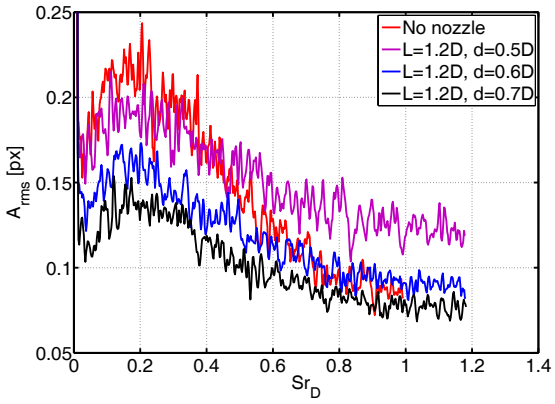

Figure 16. Spectrum of the oscillating recompression shock for different nozzle diameters

important to know for the design of space launchers. Furthermore, the measurement results show evidence of an azimuthal mode. Measurements concerning the recompression shock indicate an independence from the inner dynamic of the base flow because it oscillates with $Sr = 0.2$ independently of the nozzle configuration. Future work will focus on the improvement of the spatial resolution of the base-pressure fluctuations. At the same time, the identification of the Strouhal numbers and azimuthal modes will be targeted with a sting supported model. Thus, the influence of a strut is avoided. In the longer run, experiments with hot jets will be executed where the flow parameters will additionally be measured with PIV.

Acknowledgments

Financial support has been provided by the German Research Foundation (Deutsche Forschungsgemeinschaft – DFG) in the framework of the Sonderforschungsbereich Transregio 40. The help and the advice of the technical stuff of the supersonic and hypersonic department is gratefully acknowledged. Some measurement equipment has been kindly provided by the Institute of Aeronautics and Astronautics, RWTH Aachen.

References

[1]Rollstin, L. *Measurement of Inflight Base-Pressure on an Artiellery-Fired Projectile*. AIAA Paper 87-2427, 1987.

[2]Meiss, J.-H. and Schröder, W. *Large-Eddy Simulation of a Generic Space Vehicle*. In: A. Gülhan (ed.), RESPACE - Key Technologies for Reusable Space Systems, Springer-Verlag Berlin Heidelberg, ISBN 978-3-540-77818-9, pp. 21–39, 2008.

[3]Henckels, A. and Gülhan, A. *Experimental Study of the Base Flow*. In: A. Gülhan (ed.), RESPACE - Key Technologies for Reusable Space Systems, Springer-Verlag Berlin Heidelberg, ISBN 978-3-540-77818-9, pp. 21–39, 2008.

[4]Eldred, K. *Base Pressure Fluctuations*. Journal of the Acoustical Society of America, Vol. **33**(1), pp. 59–63, 1961.

[5]Mabey, D. G. *Some Measurements of Base Pressure Fluctuations at Subsonic and Supersonic Speeds*. Aeronautical Research Council, ARC-CP-1204, 1972; also Royal Aircraft Establishment, RAE-TR-70148, Bedford, England, U.K., August 1970.

[6]Shvets, A. I. *Base Pressure Fluctuations*. Fluid Danamics, Vol. **14**(3) 1979, pp. 394–401, 1979.

[7]Délery, J. and Sirieux, M. *Base Flows behind Missiles*. AGARD LS-98, T.P. n°1979-14E, 1979.

[8]Herrin, J. L. and Dutton, J. C. *The Turbulence Structure of a Reattaching Axisymmetric Compressible Free Shear Layer*. Physics of Fluids, **9**(11), pp. 3502–3512, 1997.

[9]Bourdon, C. J. and Dutton, J. C. *Visualizations and Measurements of Axisymmetric Base Flows Altered by Surface Disturbances*. AIAA 2001-0286, 2001.

[10]Cannon, P. M., Gregory, S. E. and Dutton, J. C. *Time-Series Analysis Axisymmetric Base-Pressure Measurements with Simultaneous Near-Wake Planar Visualizations*. 35^{th} AIAA Fluid Dynamics Conference and Exhibit, AIAA Paper 2005-5285, 2005.

[11]Janssen, J. R. and Dutton, J. C. *Time-Series Analysis of Supersonic Base-Pressure Fluctuations*. AIAA Journal, **42**(3), 605–613, 2004.

[12]Janssen, J. R. and Dutton, J. C. *Sub-Boundary-Layer Disturbance Effects on Supersonic Base-Pressure Fluctuations*. Journal of Spacecraft and Rockets Press, **42**(6), 1017–1024, 2005.

[13]Deprés, D., Reijasse, P. and Dussauge, J. P. *Analysis of Unsteadiness in Afterbody Transonic Flows*. AIAA Journal, **42**(12), 2541–2550, 2004.

[14]Dépres, D, Radulovic, S. and Lambare, H. *Reduction of Unsteady Effects in Afterbody Transonic Flows*. 6^{th} International Symposium on Launcher Technologies, Munich, 2005.

[15]David, C. and Radulovic, S. *Prediction of Buffet Loads on the Ariane 5 Afterbody*. 6^{th} International Symposium on Launcher Technologies, Munich, 2005.

[16]Sandberg, R. D. and Fasel, H. F. *Direct Numerical Simulations of Transitional Supersonic Base Flows*. AIAA Journal, **44**(4), 848–858, 2006.

[17]Sandberg, R. D. and Fasel, H. F. *Numerical Investigation of Transitional Supersonic Axisymmetric Wakes*. Journal of Fluid Mechanics, **563**, 1–41, 2006.

[18]Simon, F., Deck, S., Guillen, P., Sagaut, P. and Merlen, A. *Numerical Simulation of the Compressible Mixing Layer Past an Axisymmetric Trailing Edge*. Journal of Fluid Mechanics, **591**, 215–253, 2007.

[19]Deck, S. and Thorigny, P. *Unsteadiness of an Axisymmetric Separating-Reattaching Flow: Numerical Investigation*. Physics of Fluids, **19**(6), 1017–1024, 2007.

[20]Weiss, P.-É, Deck, S. Robinet, J.-C. and Sagaut, P. *On the Dynamics of Axisymmetric Turbulent Separating/Reattaching Flows*. AIAA Journal, **42**(3), 605–613, 2009.

[21]Neeb, D. *Experimentelle Untersuchung der Heckströmung einer Boosterkonfiguraion im Hyperschall*. Diplomarbeit at the German Aerospace Center, Institute of Aerodynamics and Flow Technology, Supersonic and Hypersonic Technology Department, Cologne supervised by RWTH Aachen, Chair of Fluid Mechanics and Institute of Aerodynamics, 2007.